

A New P2-Type Layered Oxide Cathode with Extremely High Energy Density for Sodium-Ion Batteries

Jang-Yeon Hwang, Jongsoon Kim, Tae-Yeon Yu, and Yang-Kook Sun*

Herein, a new P2-type layered oxide is proposed as an outstanding intercalation cathode material for high energy density sodium-ion batteries (SIBs). On the basis of the stoichiometry of sodium and transition metals, the P2-type $\text{Na}_{0.55}[\text{Ni}_{0.1}\text{Fe}_{0.1}\text{Mn}_{0.8}]\text{O}_2$ cathode is synthesized without impurities phase by partially substituting Ni and Fe into the Mn sites. The partial substitution results in a smoothing of the electrochemical charge/discharge profiles and thus greatly improves the battery performance. The P2-type $\text{Na}_{0.55}[\text{Ni}_{0.1}\text{Fe}_{0.1}\text{Mn}_{0.8}]\text{O}_2$ cathode delivers an extremely high discharge capacity of 221.5 mAh g^{-1} with a high average potential of $\approx 2.9 \text{ V}$ (vs Na/Na^+) for SIBs. In addition, the fast Na-ion transport in the P2-type $\text{Na}_{0.55}[\text{Ni}_{0.1}\text{Fe}_{0.1}\text{Mn}_{0.8}]\text{O}_2$ cathode structure enables good power capability with an extremely high current density of 2400 mA g^{-1} (full charge/discharge in 12 min) and long-term cycling stability with $\approx 80\%$ capacity retention after 500 cycles at 600 mA g^{-1} . A combination of electrochemical profiles, in operando synchrotron X-ray diffraction analysis, and first-principles calculations are used to understand the overall Na storage mechanism of P2-type $\text{Na}_{0.55}[\text{Ni}_{0.1}\text{Fe}_{0.1}\text{Mn}_{0.8}]\text{O}_2$.

Recently, sodium-ion batteries (SIBs) have attracted considerable interest as an excellent alternative to LIBs.^[3–5] Sodium follows lithium in the alkali metal series and possesses chemical properties similar to those of lithium; this initially suggested that SIBs could operate with the same battery components and electrical storage mechanism as LIBs. In addition, sodium is one of the most abundant elements in the earth's crust, making SIBs a potentially viable technology. Over the past few years, sodium insertion materials have been extensively studied as promising candidates for use as cathodes in SIBs; P2-type Na_xMeO_2 (P2- Na_xMeO_2 , where Me is a transition metal and $x \leq 0.7$) cathodes reportedly exhibit higher energy density than other cathode materials for SIBs.^[6,7] In particular, manganese-based P2-type Na_xMeO_2 attracted considerable attention as a promising cathode material in SIBs due to its low-cost battery system without sacrificing energy density and safety.^[8]

1. Introduction

Over the past few decades, battery technologies have become a key component of our daily activities because of their increasingly powerful capabilities. In particular, lithium-ion batteries (LIBs) represent the main power source used in portable devices and electric vehicles (EVs) owing to their high energy density and ecofriendly operation.^[1] These favorable features have resulted in an explosive growth in the global demand for LIBs. However, the high cost of cobalt and lithium used as raw materials in LIBs represent a serious issue.^[2] Concerns related to the scarcity of these raw materials are the driving force for the development of new types of electrical energy storage systems with low cost and high environmental sustainability.

In general, the valence state of Mn considerably affects the polymorphism of manganese-based P2-type Na_xMeO_2 compounds. Komaba and co-workers recently introduced the P'2- $\text{Na}_{0.64}\text{Mn}^{(3.37+)}\text{O}_2$ compound (where the prime symbol denotes a distorted polymorph with an orthorhombic lattice), which is the optimized single phase of P2- Na_xMnO_2 without vacant Mn sites.^[9] However, P'2- $\text{Na}_{0.64}\text{MnO}_2$ exhibited complicated stepwise voltage profiles corresponding to multiple phase transitions upon sodiation–desodiation processes. Similar electrochemical behaviors were also observed for P'2- $\text{Na}_{0.67}\text{MnO}_2$ by Bruce and co-workers;^[10] this may be a major drawback for the application of these materials as a cathode in SIBs. On the other hand, pure P2-type Na_xMnO_2 compound without the orthorhombic lattice, $\text{Na}_{0.59}\text{Mn}_{0.9}^{(3.76+)}\text{O}_2$, was proposed by Komaba and co-workers.^[9] The $\text{Na}_{0.59}\text{Mn}_{0.9}^{(3.76+)}\text{O}_2$ shows relatively smooth voltage profiles; however, its cycling stability were unsatisfactory because of Mn vacancy ordering in the structure. In addition, sensitivity of the synthesis, including a slow cooling process and high oxygen pressures after heating at high temperature ($\approx 1000 \text{ }^\circ\text{C}$), is required for the preparation of these P2- Na_xMnO_2 compounds.^[9–12] To address these issues, a number of studies have focused on the structural stabilization of P2-type Na_xMnO_2 by controlling the oxidation state of Mn, for instance, by substituting or doping of different metals (Li,^[13] Ni,^[14,15] Fe,^[16] and Mg^[17]) into the Mn sites; however, most compounds still suffer from low specific capacity and

Dr. J.-Y. Hwang, T.-Y. Yu, Prof. Y.-K. Sun
Department of Energy Engineering
Hanyang University
Seoul 04763, Republic of Korea
E-mail: yksun@hanyang.ac.kr

Prof. J. Kim
Department of Nano Science and Technology
Sejong University
Seoul 05006, Republic of Korea

 The ORCID identification number(s) for the author(s) of this article can be found under <https://doi.org/10.1002/aenm.201803346>.

DOI: 10.1002/aenm.201803346

poor cycling stability. Therefore, the development of efficient manganese-based P2-type Na_xMeO_2 cathode materials that can withstand repeated extractions/insertions of the large Na^+ ions without loss of structural stability remains a critical issue.

Accordingly, we aimed to develop manganese-based P2- Na_xMeO_2 materials as effective intercalation host for low cost and high energy density SIBs. In the previous reports, it was found that the high Mn oxidation state should be required to prepare not P'2- Na_xMnO_2 but P2- Na_xMnO_2 . Namely, this implies the importance of control of Mn oxidation state to prepare manganese-based pure P2- Na_xMeO_2 . On the basis of the stoichiometry of sodium and transition metals, we designed and synthesized a pure P2-type layered oxide cathode, $\text{Na}_{0.55}[\text{Ni}_{0.1}^{(2+)}\text{Fe}_{0.1}^{(3+)}\text{Mn}_{0.8}^{(3.7+)}]\text{O}_2$ (P2- $\text{Na}_{0.55}[\text{Ni}_{0.1}\text{Fe}_{0.1}\text{Mn}_{0.8}]\text{O}_2$), without impurity phase by partially substituting Ni and Fe into the Mn sites. The P2- $\text{Na}_{0.55}[\text{Ni}_{0.1}\text{Fe}_{0.1}\text{Mn}_{0.8}]\text{O}_2$ cathode notably exhibited a high specific capacity of $\approx 221.5 \text{ mAh g}^{-1}$ with an average potential of 2.9 V in the voltage range of 1.5–4.3 V for SIBs. In addition, P2- $\text{Na}_{0.55}[\text{Ni}_{0.1}\text{Fe}_{0.1}\text{Mn}_{0.8}]\text{O}_2$ exhibited an outstanding cycling stability with $\approx 75\%$ capacity retention over 100 cycles at a 0.5 C rate. Even at a high current density of 2400 mA g^{-1} , the cathode still delivered a specific capacity of 85 mAh g^{-1} , which demonstrates the excellent power capability of P2- $\text{Na}_{0.55}[\text{Ni}_{0.1}\text{Fe}_{0.1}\text{Mn}_{0.8}]\text{O}_2$, highlighting its promising potential as cathode in SIBs. The overall reaction mechanism of P2- $\text{Na}_{0.55}[\text{Ni}_{0.1}\text{Fe}_{0.1}\text{Mn}_{0.8}]\text{O}_2$ was clearly identified through a combination of first-principles calculation and experiments.

2. Results and Discussion

2.1. Synthesis and Characterization

P2- $\text{Na}_{0.55}[\text{Ni}_{0.1}\text{Fe}_{0.1}\text{Mn}_{0.8}]\text{O}_2$ was synthesized via a typical solid-state method and obtained by quenching from 950°C without a slow cooling process. Structural information on P2- $\text{Na}_{0.55}[\text{Ni}_{0.1}\text{Fe}_{0.1}\text{Mn}_{0.8}]\text{O}_2$ was analyzed by X-ray diffraction (XRD) with Rietveld refinement.^[18] As shown in Figure 1a, $\text{Na}_{0.55}[\text{Ni}_{0.1}\text{Fe}_{0.1}\text{Mn}_{0.8}]\text{O}_2$ showed a pure rhombohedral structure belonging to the $P6_3/mmc$ space group without any impurities or secondary phases.^[19] The Rietveld refinement of the XRD pattern of P2- $\text{Na}_{0.55}[\text{Ni}_{0.1}\text{Fe}_{0.1}\text{Mn}_{0.8}]\text{O}_2$ yielded lattice parameters a and c of 2.90194(5) and 11.2601(4) Å, respectively. Detailed structural data on P2- $\text{Na}_{0.55}[\text{Ni}_{0.1}\text{Fe}_{0.1}\text{Mn}_{0.8}]\text{O}_2$, such as atomic positions, isotropic parameters (B_{iso}), and occupancy with the preferred orientation parameter, are listed in Table S1 in the Supporting Information. From refinement data, it was also verified that 0.1 mol of Ni and Fe ions were substituted in the Mn sites and that ≈ 0.55 mol of Na ions were introduced in the structure, which matches well with inductively coupled plasma (ICP) results for $\text{Na}_{0.55}[\text{Ni}_{0.1}\text{Fe}_{0.1}\text{Mn}_{0.8}]\text{O}_2$. The accuracy of the structural model obtained by Rietveld refinement was confirmed by the small reliability factors ($R_p = 1.01\%$, $R_1 = 5.88\%$, $R_F = 6.12\%$, and $\chi^2 = 4.33\%$). Transmission electron microscopy-energy dispersive X-ray spectroscopy (TEM-EDX) elementary mapping, as displayed in Figure 1b, indicates that the sodium, nickel, iron, manganese, and oxygen elements are uniformly

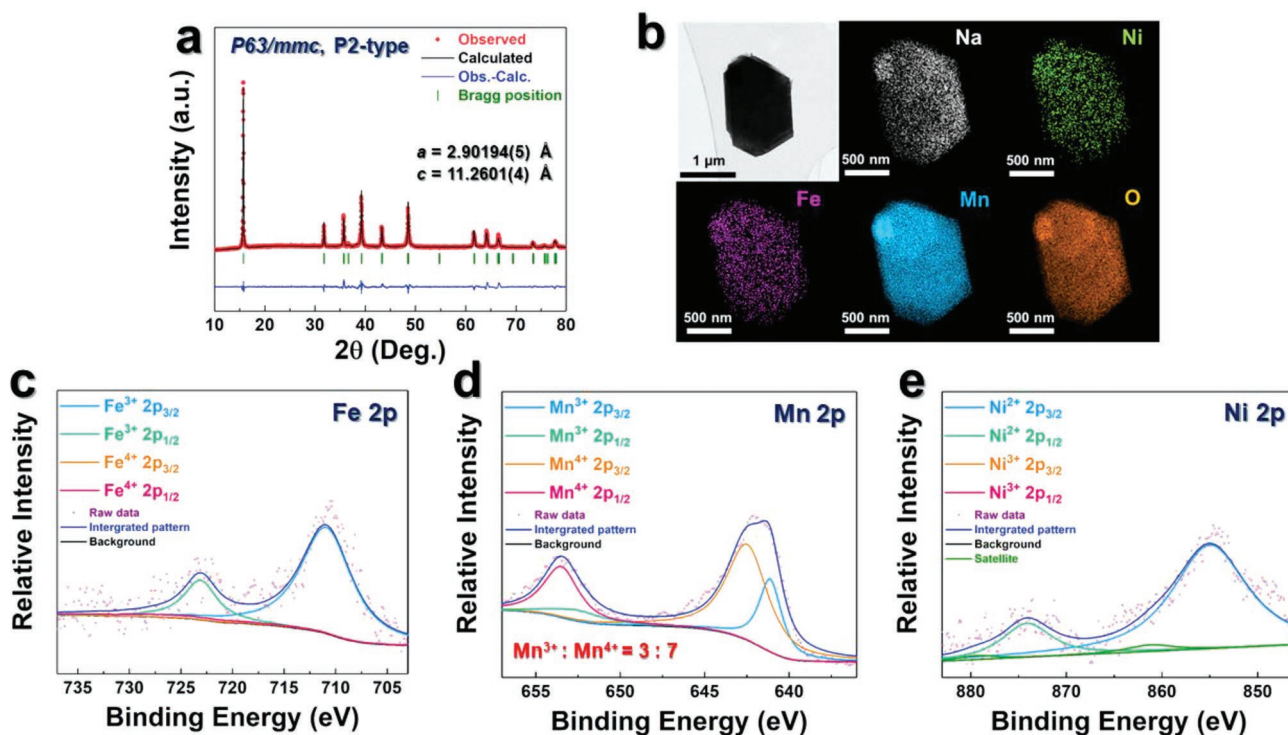


Figure 1. a) Profile-matched XRD patterns of P2- $\text{Na}_{0.55}[\text{Ni}_{0.1}\text{Fe}_{0.1}\text{Mn}_{0.8}]\text{O}_2$ calculated using the Rietveld refinement method ($R_p = 1.01\%$, $R_1 = 5.88\%$, $R_F = 6.12\%$, and $\chi^2 = 4.33\%$). b) TEM image and corresponding EDX mappings of P2- $\text{Na}_{0.55}[\text{Ni}_{0.1}\text{Fe}_{0.1}\text{Mn}_{0.8}]\text{O}_2$ (white color: sodium, green color: nickel, violet color: iron, blue color: manganese, orange color: oxygen). XPS spectra of the c) Fe 2p, d) Mn 2p regions, and e) Ni 2p region for the as-prepared P2- $\text{Na}_{0.55}[\text{Ni}_{0.1}\text{Fe}_{0.1}\text{Mn}_{0.8}]\text{O}_2$.

distributed in the sample. In addition, the Na:Ni:Fe:Mn atomic ratios in P2-Na_{0.55}[Ni_{0.1}Fe_{0.1}Mn_{0.8}]O₂ were further estimated to be 0.552:0.102:0.101:0.797 by TEM-EDX measurements, which is well matched with the atomic ratios measured through ICP analyses. For comparison, P'2-Na_{0.67}MnO₂ was synthesized via the same synthesis procedure. P'2-Na_{0.67}MnO₂ was refined in the orthorhombic (*Cmcm*) space group (Figure S1 and Table S2, Supporting Information), in good agreement with the previously reported data.^[12] In this case, TEM-EDX measurements yielded a Na:Mn atomic ratio of 0.6703:0.9997 (Figure S2, Supporting Information). In Figure 1b and Figure S2 in the Supporting Information, we confirmed that P2-Na_{0.55}[Ni_{0.1}Fe_{0.1}Mn_{0.8}]O₂ and P'2-Na_{0.67}MnO₂ have a size of 1–1.5 μm with plate-like morphology. X-ray photoelectron spectroscopy (XPS) measurements were used to verify the oxidation state of each transition metal, such as Mn, Fe, and Ni, in the as-prepared P2-Na_{0.55}[Ni_{0.1}Fe_{0.1}Mn_{0.8}]O₂ compounds (Figure 1c–e) and P'2-Na_{0.67}MnO₂ (Figure S3, Supporting Information). The binding energy of Ni was similar to those of divalent Ni (Ni 2p_{3/2}, 854–854.7 eV),^[20,21] whereas the binding energy of Mn was intermediate between those of the trivalent (Mn 2p_{3/2}, 641.2 eV) and tetravalent (Mn 2p_{3/2}, 642.6 eV) state although considerably close to that of the tetravalent state (Figure 1e).^[22,23] The Fe 2p_{3/2} peak at ≈710.8 eV indicates the presence of Fe in Fe³⁺ form (Figure 1d).^[24,25] In the case of P'2-Na_{0.67}MnO₂, the binding energy of Mn was intermediate between those of the trivalent (Mn 2p_{3/2}, 642.6 eV) and tetravalent (Mn 2p_{3/2}, 642.6 eV) state although considerably close to that of the trivalent state. Combining the ICP and XPS results, the chemical formulas of the P'2-Na_{0.67}MnO₂ and P2-Na_{0.55}[Ni_{0.1}Fe_{0.1}Mn_{0.8}]O₂ compounds could be determined as

Na_{0.67}Mn^(3.5+)O₂ and Na_{0.55}[Ni_{0.1}⁽²⁺⁾Fe_{0.1}⁽³⁺⁾Mn_{0.8}^(3.7+)]O₂, respectively. The above analysis proves our idea for the structural design of P2-Na_{0.55}[Ni_{0.1}Fe_{0.1}Mn_{0.8}]O₂ to be reasonable and further confirms the feasibility of the present approach for successful synthesis of the Mn-based pure P2-type layered oxide cathode material.

2.2. Electrochemical Performance

We compared the electrochemical Na storage performances of P'2-Na_{0.67}MnO₂ and P2-Na_{0.55}[Ni_{0.1}Fe_{0.1}Mn_{0.8}]O₂ measured for Na metal | 0.5 M NaPF₆ in propylene carbonate with fluoroethylene carbonate 2 vol% | P'2-Na_{0.67}MnO₂ or P2-Na_{0.55}[Ni_{0.1}Fe_{0.1}Mn_{0.8}]O₂ cells. All cells were tested in the voltage range of 1.5–4.3 V at 30 °C. As shown in Figure 2a, P2-Na_{0.55}[Ni_{0.1}Fe_{0.1}Mn_{0.8}]O₂ delivered a high discharge capacity of ≈221.5 mAh g⁻¹ at 12 mA g⁻¹. In contrast, P'2-Na_{0.67}MnO₂ delivered a relatively low discharge capacity of 198 mAh g⁻¹ under the same test conditions (Figure 2b), which is similar to the value previously reported by Bruce and co-workers.^[10] The charge–discharge curves and corresponding dQ dV⁻¹ plots (Figure 2a and inset) show that P2-Na_{0.55}[Ni_{0.1}Fe_{0.1}Mn_{0.8}]O₂ exhibited smooth charge–discharge curves, with less phase transitions; however, the charge–discharge curves and corresponding dQ dV⁻¹ plots of P'2-Na_{0.67}MnO₂ (Figure 2b and inset) involve complex voltage plateaus and steps upon sodiation–desodiation. We suggest that the smooth electrochemistry of P2-Na_{0.55}[Ni_{0.1}Fe_{0.1}Mn_{0.8}]O₂ might be attributed to the formation of a highly stable framework, suppressing structural transitions during the sodiation–desodiation processes and resulting

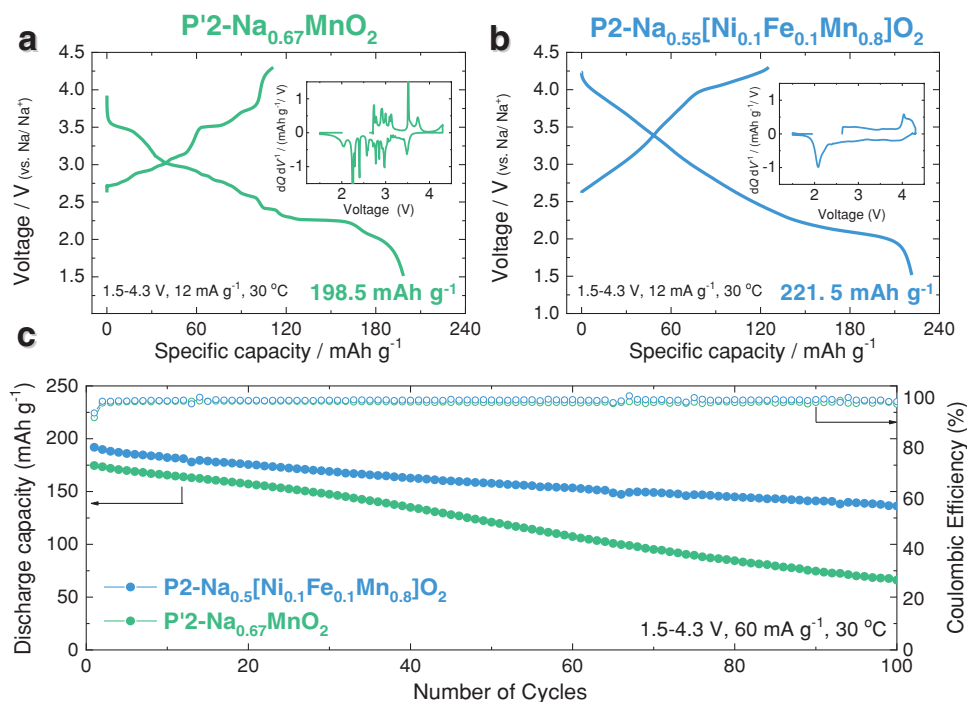


Figure 2. Comparison of the electrochemical performances of P'2-Na_{0.67}MnO₂ and P2-Na_{0.55}[Ni_{0.1}Fe_{0.1}Mn_{0.8}]O₂. Charge–discharge profiles and corresponding dQ dV⁻¹ plots (inset) of a) P'2-Na_{0.67}MnO₂ and b) P2-Na_{0.55}[Ni_{0.1}Fe_{0.1}Mn_{0.8}]O₂ at a current density of 12 mA g⁻¹. c) Results of cycling tests at a current density of 60 mA g⁻¹. All cells were tested using 2032 coin-type cell in the voltage range of 1.5–4.3 V, at 30 °C.

in improved cycling stability.^[10] Moreover, it was reported that Jahn–Teller distortion by $\text{Mn}^{3+}/\text{Mn}^{4+}$ redox reaction results in large/anisotropic volume change and long-range ordering of Na^+ /vacancies;^[9] thus, this implies that particular Na^+ /vacancy configuration for each Na_xMnO_2 ($0 < x < 1$) composition should be required to lower the structural instability by the Jahn–Teller distortion during charging/discharging. Hence, it could be supposed that the charge/discharge voltage profiles of Na_xMnO_2 consisted of multiple steps owing to the changes of long-range ordering of Na^+ /vacancies in the Na_xMnO_2 structure. However, the existence of Fe and Ni in the structure enables to suppress the Jahn–Teller distortion of Mn^{3+} , which may result in more smooth electrochemistry of the $\text{Na}_x[\text{Ni}_{0.1}\text{Fe}_{0.1}\text{Mn}_{0.8}]\text{O}_2$ than that of the Na_xMnO_2 . To prove this phenomenon, we computed the Mn–O bonding distances of $\text{P}2\text{-Na}_1\text{Mn}^{(3+)}\text{O}_2$ and $\text{P}2\text{-Na}_1[\text{Ni}_{0.1}\text{Fe}_{0.1}\text{Mn}_{0.8}^{(3+)}]\text{O}_2$ through first-principles calculation. As shown in Figure S4 in the Supporting information, all the Mn–O bonding distances for $\text{P}2\text{-Na}_1[\text{Ni}_{0.1}\text{Fe}_{0.1}\text{Mn}_{0.8}]\text{O}_2$ are very similar whereas the two Mn–O bonding distances (Mn2–O8 and Mn2–O11) for $\text{P}2\text{-Na}_1\text{MnO}_2$ are particularly larger than the others. Hence, we supposed that the similar Mn–O bonding distances for $\text{Na}_1[\text{Ni}_{0.1}\text{Fe}_{0.1}\text{Mn}_{0.8}]\text{O}_2$ was possible because of the Ni and Fe substitution of partial Mn^{3+} in the crystal structure, which is thought to have suppressed the cooperative Jahn–Teller distortion. As expected, $\text{P}2\text{-Na}_{0.55}[\text{Ni}_{0.1}\text{Fe}_{0.1}\text{Mn}_{0.8}]\text{O}_2$ exhibited outstanding cycling stability, with a capacity retention of 75% after 100 cycles, whereas the discharge capacity of $\text{P}2\text{-Na}_{0.67}\text{MnO}_2$ rapidly decreased to $\approx 37\%$ of the initial discharge capacity under the same test conditions (Figure 2c).

2.3. Structural Evolution Study via In Operando Synchrotron XRD Analysis

To gain better insight into the Na storage behavior and crystal structure changes of $\text{P}2\text{-Na}_{0.55}[\text{Ni}_{0.1}\text{Fe}_{0.1}\text{Mn}_{0.8}]\text{O}_2$, in operando synchrotron XRD measurement was performed during

the initial charge (sodiation)–discharge (desodiation) process, and the results are displayed in Figure 3. Over a wide range of Na contents in the $\text{P}2\text{-Na}_x[\text{Ni}_{0.1}\text{Fe}_{0.1}\text{Mn}_{0.8}]\text{O}_2$ structure ($0.1 \leq x \leq 0.9$), a continuous reversible shift of the XRD peaks was observed during Na (de)intercalation process. During the first charge process (desodiation), the P2 (002) and P2 (004) diffraction peaks in the XRD pattern showed a monotonic shift toward lower angles, whereas the P2 (100) and P2 (102) peaks gradually shifted toward higher angles. On extracting ≈ 0.3 mol of Na ions from the crystal structure (charged at 4.1 V), $\text{Na}_x[\text{Ni}_{0.1}\text{Fe}_{0.1}\text{Mn}_{0.8}]\text{O}_2$ underwent a phase transition from the P2-type structure. With a further voltage increase in the 4.1–4.3 V range, the XRD pattern changed and the structure could be indexed to the OP4-type $\text{Na}_x[\text{Ni}_{0.1}\text{Fe}_{0.1}\text{Mn}_{0.8}]\text{O}_2$ with the $P6m2$ space group, as reported in previous studies.^[16,26–28] When Na ions are deintercalated from the structure, c -lattice parameter of the $\text{P}2\text{-Na}_x[\text{Ni}_{0.1}\text{Fe}_{0.1}\text{Mn}_{0.8}]\text{O}_2$ is increased due to $\text{O}^{2-}\text{-O}^{2-}$ repulsion, which results in structural instability of the $\text{P}2\text{-Na}_{0.55}[\text{Ni}_{0.1}\text{Fe}_{0.1}\text{Mn}_{0.8}]\text{O}_2$ consequently. At the high state of charge states, the crystal structure of $\text{P}2\text{-Na}_{0.55}[\text{Ni}_{0.1}\text{Fe}_{0.1}\text{Mn}_{0.8}]\text{O}_2$ becomes increasingly unstable; consequently, the phase transition from P2 to OP4 phase would be occurred because of the thermodynamically instable prismatic sites without Na ions.^[16] This phenomenon is analogous to O1–O3 phase transition occurred at $\text{O}3\text{-LiCoO}_2$.^[29,30] Because OP4 phase has not only prismatic sites but also octahedral sites, the phase transition from P2 to OP4 enables to lower the structural instability of $\text{Na}_x[\text{Ni}_{0.1}\text{Fe}_{0.1}\text{Mn}_{0.8}]\text{O}_2$ without lengthening the c -lattice parameter, which implies that during Na deintercalation process, c -lattice parameter of $\text{Na}_x[\text{Ni}_{0.1}\text{Fe}_{0.1}\text{Mn}_{0.8}]\text{O}_2$ might be decreased after P2–OP4 phase transition. The P2–OP4 phase transition was found to be highly reversible during Na^+ ion intercalation process. During discharging to 4.1 V, the intensity of the XRD peaks corresponding to the OP4 phase gradually decreased with increasing sodium content. The peaks corresponding to OP4 completely disappeared, and the P2 phase reappeared until ≈ 2.0 V. Finally, the last stage of the discharge from 2.0 to

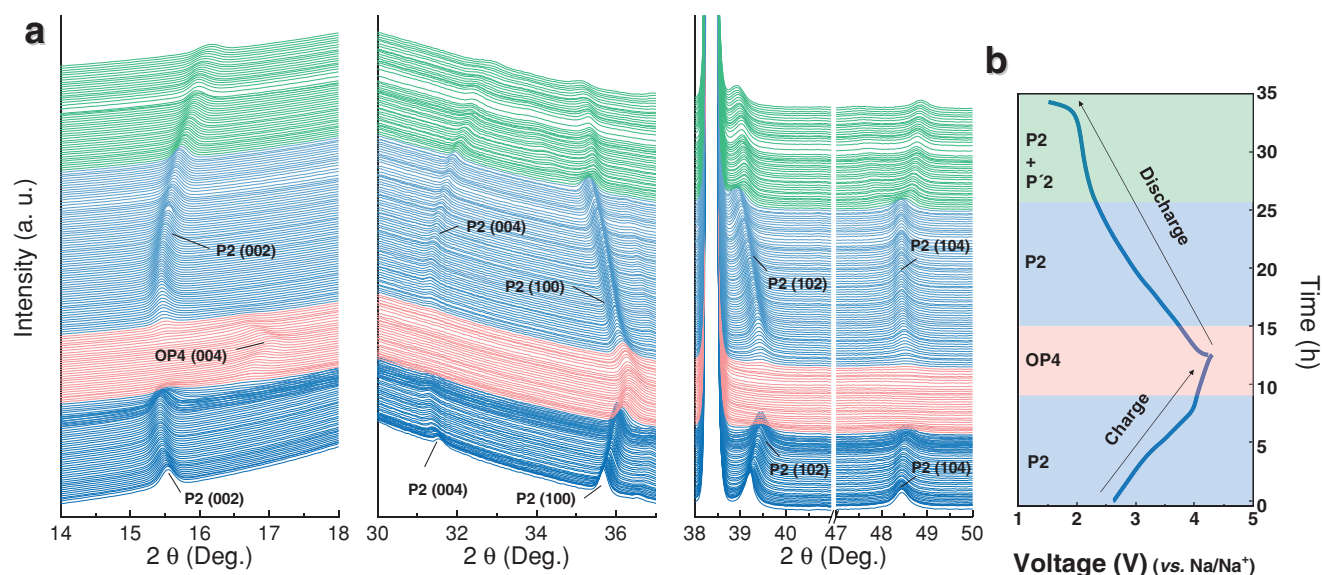


Figure 3. a) In operando synchrotron XRD patterns and b) corresponding charge–discharge curves of $\text{P}2\text{-Na}_{0.55}[\text{Ni}_{0.1}\text{Fe}_{0.1}\text{Mn}_{0.8}]\text{O}_2$.

1.5 V showed a slightly complex behavior, corresponding to a biphasic mechanism involving a major P2-type hexagonal phase and a minor orthorhombic phase. These structural changes phenomenon is usually observed in Mn-rich P2-type layered oxide cathodes of SIBs, owing to the increase in the amount of Mn³⁺ ions during deep discharge at 2.0 V (vs Na/Na⁺).^[27] On the other hand, we observed the XRD peak-broadening of P2-Na_x[Ni_{0.1}Fe_{0.1}Mn_{0.8}]O₂ before P2/OP4 phase transition. During Na deintercalation from the structure, the slab distance on Na sites at P2-Na_x[Ni_{0.1}Fe_{0.1}Mn_{0.8}]O₂ and its *c*-lattice parameters get larger. When the Na amounts in P2-Na_x[Ni_{0.1}Fe_{0.1}Mn_{0.8}]O₂ are lower than 0.25 mol, it experiences the phase transition from P2 (ABBA sequencing) to OP4 (ABBACAAC sequencing). Thus, it is supposed that this large structural change of P2-Na_x[Ni_{0.1}Fe_{0.1}Mn_{0.8}]O₂ resulting from the phase transition may affect broadening the XRD peaks of P2-Na_x[Ni_{0.1}Fe_{0.1}Mn_{0.8}]O₂. However, when Na ions are reintercalated into the structure, OP4 phase is recharged to P2 phase and the broadened XRD peaks return to the original sharp peaks. As shown TEM images (Figure S5 in the Supporting Information), despite the large changes in crystal structure, P2-Na_{0.55}[Ni_{0.1}Fe_{0.1}Mn_{0.8}]O₂ can survive without serious damage to its morphology during repeated charge-discharge process.

2.4. Investigation of Na Storage Mechanism via First-Principles Calculation

First-principles calculation was carried out to investigate in detail the Na storage mechanism and structural evolution of P2-Na_{0.55}[Ni_{0.1}Fe_{0.1}Mn_{0.8}]O₂ during the charge–discharge process. Using the structural information obtained by the Rietveld refinement, we calculated the formation energies and the theoretical redox potential range of P2-Na_x[Ni_{0.1}Fe_{0.1}Mn_{0.8}]O₂ (0 ≤ *x* ≤ 1) and OP4-Na_x[Ni_{0.1}Fe_{0.1}Mn_{0.8}]O₂ (0 ≤ *x* ≤ 0.25). The predicted theoretical redox potential of the P2- or OP4-Na_x[Ni_{0.1}Fe_{0.1}Mn_{0.8}]O₂ (P2-/OP4-Na_x[Ni_{0.1}Fe_{0.1}Mn_{0.8}]O₂) materials was calculated using the following equation

$$V = -\frac{E[\text{Na}_{x_2}\text{NFMO}_2] - E[\text{Na}_{x_1}\text{NFMO}_2] - (x_2 - x_1)E(\text{Na})}{(x_2 - x_1)F} \quad (1)$$

where *V* is the average redox potential in the *x*₁ ≤ *x* ≤ *x*₂ compositional range and *E*[Na_{*x*}[Ni_{0.1}Fe_{0.1}Mn_{0.8}]O₂] is the density functional theory (DFT) energy of the most stable configuration of P2-/OP4-Na_{*x*}[Ni_{0.1}Fe_{0.1}Mn_{0.8}]O₂ at each composition. Na_{*x*}[Ni_{0.1}Fe_{0.1}Mn_{0.8}]O₂ is labeled as Na_{*x*}NFMO₂ in the equation. *E*(Na) is the energy of the Na metal and *F* is the Faraday constant. Additionally, as tabulated in Table S1 in the Supporting Information, there are two sites for Na ions and one site for transition metals such as Mn, Ni, and Fe in the P2-Na_{*x*}[Ni_{0.1}Fe_{0.1}Mn_{0.8}]O₂ crystal structure, which means that 2 mol Na ions can be theoretically intercalated into the 2-Na_{*x*}[Ni_{0.1}Fe_{0.1}Mn_{0.8}]O₂ structure. Note that it is not meaningful for real operation condition of SIB due to requirement of too low voltage for intercalation of 2 mol Na ions in the P2-Na_{*x*}[Ni_{0.1}Fe_{0.1}Mn_{0.8}]O₂ structure. However, because of the preparation of the various Na/vacancy configurations based on the fully sodiated

P2-Na₂[Ni_{0.1}Fe_{0.1}Mn_{0.8}]O₂ structure, numerous Na/vacancy configuration of 1 mol Na intercalated P2-Na₁[Ni_{0.1}Fe_{0.1}Mn_{0.8}]O₂ structure could be generated, unlike the fully desodiated P2-Na₀[Ni_{0.1}Fe_{0.1}Mn_{0.8}]O₂ structure. Figure 4a presents the convex hull plot of the formation energy of P2-/OP4-Na_{*x*}NFMO₂ (0 ≤ *x* ≤ 1) as a function of the Na content; this calculation was approximate due to the presence of several stable intermediate phases of P2-/OP4-Na_{*x*}[Ni_{0.1}Fe_{0.1}Mn_{0.8}]O₂ between Na₁[Ni_{0.1}Fe_{0.1}Mn_{0.8}]O₂ and Na₀[Ni_{0.1}Fe_{0.1}Mn_{0.8}]O₂ during the solid-solution reaction. In particular, when the Na amount in Na_{*x*}NFMO₂ was less than ≈0.25 mol, the OP4 phase was more stable than the P2 phase, in good agreement with the in operando XRD results on the phase transition from P2-Na_{*x*}[Ni_{0.1}Fe_{0.1}Mn_{0.8}]O₂ to OP4-Na_{*x*}[Ni_{0.1}Fe_{0.1}Mn_{0.8}]O₂. The predicted redox potential range of the P2- and OP4-Na_{*x*}NFMO₂ materials as a function of the Na content (0 ≤ *x* ≤ 1) shows that most of Na ions in the Na_{*x*}NFMO₂ structure could be (de)intercalated in the voltage range between 1.5 and 4.3 V (vs Na⁺/Na). The plot of the predicted voltage of P2- and OP4-Na_{*x*}[Ni_{0.1}Fe_{0.1}Mn_{0.8}]O₂ is well matched with the experimentally measured galvanostatic intermittent titration technique (GITT) profile (Figure 4b). These computational results highlight that the remarkably high discharge capacity of ≈221.5 mAh g⁻¹ delivered by P2-Na_{0.55}[Ni_{0.1}Fe_{0.1}Mn_{0.8}]O₂ is reasonable.

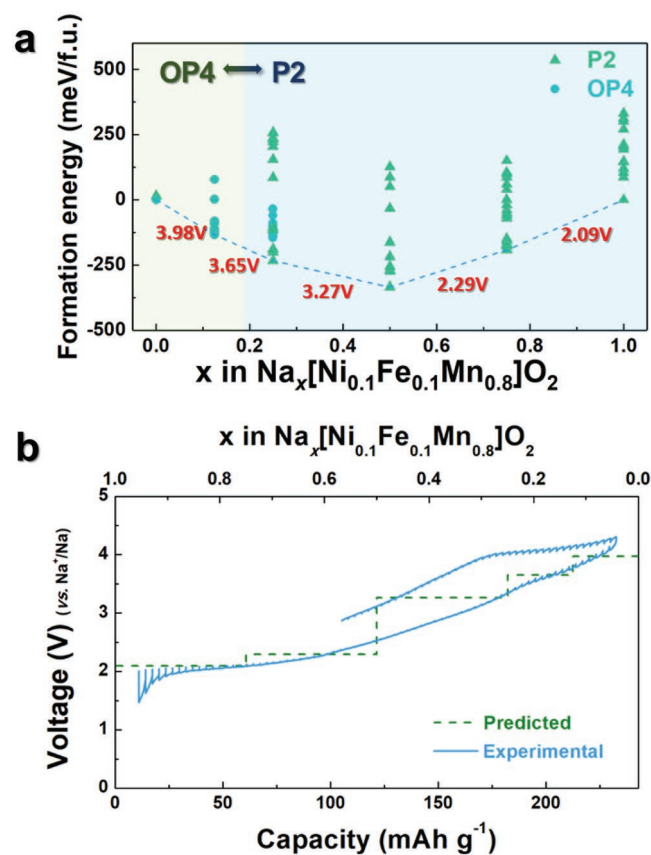


Figure 4. a) Formation energy of P2-Na_{*x*}[Ni_{0.1}Fe_{0.1}Mn_{0.8}]O₂ (0 ≤ *x* ≤ 1) and OP4-Na_{*x*}[Ni_{0.1}Fe_{0.1}Mn_{0.8}]O₂ (0 ≤ *x* ≤ 0.25); b) comparison of experimental charge–discharge curves measured by the galvanostatic intermittent titration technique (GITT) and voltage curves predicted using first-principles calculation.

The structural changes occurring in the $\text{P2-Na}_{0.55}[\text{Ni}_{0.1}\text{Fe}_{0.1}\text{Mn}_{0.8}]\text{O}_2$ compound during sodium (de)intercalation were further investigated in detail using a combination of first-principles calculation and experimental results (Figure 5). The crystal structures and corresponding c -lattice parameters of $\text{P2-Na}_x[\text{Ni}_{0.1}\text{Fe}_{0.1}\text{Mn}_{0.8}]\text{O}_2$ ($0 \leq x \leq 1$) predicted by first-principles calculation are presented in Figure 5a. When the Na contents varied between 0.25 and 1 mol, $\text{P2-Na}_x[\text{Ni}_{0.1}\text{Fe}_{0.1}\text{Mn}_{0.8}]\text{O}_2$ retained the P2-type crystal structure. Upon decreasing the Na content in the $\text{P2-Na}_x[\text{Ni}_{0.1}\text{Fe}_{0.1}\text{Mn}_{0.8}]\text{O}_2$ structure, the c -lattice parameter in the (002) plane gradually increased from ≈ 10.96 to ≈ 11.78 Å because of the $\text{O}^{2-}-\text{O}^{2-}$ repulsion arising from the formation of vacancies at Na sites.^[31] When the Na content was further decreased ($0 \leq x \leq 0.25$), $\text{P2-Na}_x[\text{Ni}_{0.1}\text{Fe}_{0.1}\text{Mn}_{0.8}]\text{O}_2$ underwent the P2-OP4 phase transition; the average distance between neighboring transition metal (TM) layers along the c -direction decreased from ≈ 5.89 ($=11.78/2$) to ≈ 5.01 ($=20.04/4$) Å. Table S3 in the Supporting Information shows the detailed structural information, such as Wyckoff position and atomic position, on the $\text{OP4-Na}_{0.125}[\text{Ni}_{0.1}\text{Fe}_{0.1}\text{Mn}_{0.8}]\text{O}_2$ structure used for calculation of the lattice parameter.^[16,32] The Vegard's law on change of average Na/vacancy slab space of $\text{P2-Na}_x[\text{Ni}_{0.1}\text{Fe}_{0.1}\text{Mn}_{0.8}]\text{O}_2$ during Na de/intercalation process strengthen further Na^+ storage mechanism on the $\text{P2-Na}_x[\text{Ni}_{0.1}\text{Fe}_{0.1}\text{Mn}_{0.8}]\text{O}_2$. As shown in Figure S6 in the

Supporting Information, the Na/vacancy slab space of $\text{P2-Na}_x[\text{Ni}_{0.1}\text{Fe}_{0.1}\text{Mn}_{0.8}]\text{O}_2$ was linearly increased (or decreased) as function of Na contents between 0.22 and 0.95 mol, indicating the solid-solution reaction of $\text{P2-Na}_x[\text{Ni}_{0.1}\text{Fe}_{0.1}\text{Mn}_{0.8}]\text{O}_2$ ($0.22 \leq x \leq 0.95$) based on the Vegard's law. When the Na content decreased below 0.125 mol, however, the $\text{P2-Na}_x[\text{Ni}_{0.1}\text{Fe}_{0.1}\text{Mn}_{0.8}]\text{O}_2$ experienced sudden changes in Na/vacancy slab space irrespective of Vegard's law, indicating a P2/OP4 biphasic reaction. To confirm the structural changes and predicted reaction mechanism for $\text{P2-Na}_x[\text{Ni}_{0.1}\text{Fe}_{0.1}\text{Mn}_{0.8}]\text{O}_2$, the values of the c -lattice parameter obtained from the first-principles calculation and the experimental results obtained by Rietveld refinement of the in operando XRD patterns are plotted in Figure 5b. The experimental c -lattice parameters of P2-/OP4-phase $\text{Na}_x[\text{Ni}_{0.1}\text{Fe}_{0.1}\text{Mn}_{0.8}]\text{O}_2$ were in good agreement with the results of the calculations. These results suggested that Na ions could be reversibly intercalated or deintercalated into or out of the $\text{Na}_{0.55}[\text{Ni}_{0.1}\text{Fe}_{0.1}\text{Mn}_{0.8}]\text{O}_2$ structure via the P2-OP4 phase transition during charge–discharge process. To verify the charge compensation mechanism of $\text{P2-Na}_x[\text{Ni}_{0.1}\text{Fe}_{0.1}\text{Mn}_{0.8}]\text{O}_2$, we performed the ex situ XPS measurement on $\text{P2-Na}_x[\text{Ni}_{0.1}\text{Fe}_{0.1}\text{Mn}_{0.8}]\text{O}_2$ as function of Na contents in the structure.^[20–25] The results clearly demonstrated that the oxidation state of transition metal ions in $\text{P2-Na}_x[\text{Ni}_{0.1}\text{Fe}_{0.1}\text{Mn}_{0.8}]\text{O}_2$, such as Mn, Fe, and Ni, were changed during charging/discharging process. As shown in Figure S7 in the Supporting Information, $\text{Fe}^{3+}/\text{Fe}^{4+}$, $\text{Mn}^{3+}/\text{Mn}^{4+}$, and $\text{Ni}^{2+}/\text{Ni}^{3+}$ redox reactions occurred during charging/discharging process of $\text{P2-Na}_x[\text{Ni}_{0.1}\text{Fe}_{0.1}\text{Mn}_{0.8}]\text{O}_2$, which indicates that these Fe-, Mn-, and Ni-based redox reactions could provide the sufficient electrons for ≈ 0.91 Na de/intercalation at $\text{P2-Na}_x[\text{Ni}_{0.1}\text{Fe}_{0.1}\text{Mn}_{0.8}]\text{O}_2$ (corresponding to the specific capacity of ≈ 221.5 mAh g^{-1}). In addition, we compared the integrated spin moments of Fe, Mn, and Ni ions between $\text{P2-Na}_1[\text{Ni}_{0.1}\text{Fe}_{0.1}\text{Mn}_{0.8}]\text{O}_2$ and $\text{OP4-Na}_{0.125}[\text{Ni}_{0.1}\text{Fe}_{0.1}\text{Mn}_{0.8}]\text{O}_2$ using first-principles calculation. As shown in Figure S8 in the Supporting Information, the total electron spin counts of Fe^{3+} , Mn^{3+} , and Ni^{2+} ions on $\text{P2-Na}_1[\text{Ni}_{0.1}\text{Fe}_{0.1}\text{Mn}_{0.8}]\text{O}_2$ were confirmed to be five, four, and two, respectively. During Na deintercalation process, the electron of Fe, Mn, and Ni metals were extracted from their 3d orbitals, resulting in oxidation of the transition metal ions in $\text{P2/OP4-Na}_x[\text{Ni}_{0.1}\text{Fe}_{0.1}\text{Mn}_{0.8}]\text{O}_2$. In summary, these results clearly demonstrated that during charging/discharging process, $\text{P2/OP4-Na}_x[\text{Ni}_{0.1}\text{Fe}_{0.1}\text{Mn}_{0.8}]\text{O}_2$ might experience $\text{Fe}^{3+}/\text{Fe}^{4+}$, $\text{Mn}^{3+}/\text{Mn}^{4+}$, and $\text{Ni}^{2+}/\text{Ni}^{3+}$ redox reactions. Moreover, it is theoretically possible that 0.1 mol Fe^{3+} ions, 0.1 mol Ni^{2+} ions, and 0.8 mol Mn^{3+} ions can provide 1 mol electron for 1 mol Na intercalation into $\text{P2-Na}_x[\text{Ni}_{0.1}\text{Fe}_{0.1}\text{Mn}_{0.8}]\text{O}_2$, implies that the oxygen-related redox reaction may not be involved at Na de/intercalation process of $\text{P2-Na}_x[\text{Ni}_{0.1}\text{Fe}_{0.1}\text{Mn}_{0.8}]\text{O}_2$.

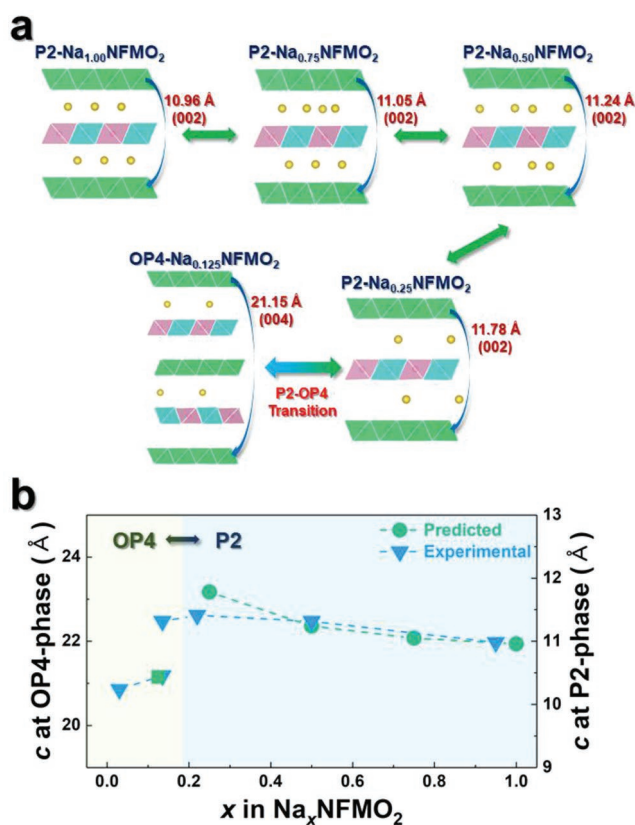


Figure 5. a) Structural changes in $\text{P2-Na}_x[\text{Ni}_{0.1}\text{Fe}_{0.1}\text{Mn}_{0.8}]\text{O}_2$ (denoted as Na_xNFM in the figure) as a function of the Na content ($0.125 \leq x \leq 1$), predicted using first-principles calculation. b) Comparison of c -lattice parameters of $\text{P2-Na}_x[\text{Ni}_{0.1}\text{Fe}_{0.1}\text{Mn}_{0.8}]\text{O}_2$ obtained by first-principles calculation with the experimental values.

2.5. Power Capability and Long-Term Cycling Stability

Figure 6a presents the rate capability of $\text{P2-Na}_{0.55}[\text{Ni}_{0.1}\text{Fe}_{0.1}\text{Mn}_{0.8}]\text{O}_2$ at various current densities ranging from 12 to 2400 mA g^{-1} . As expected from its structural stability with smooth electrochemistry, $\text{Na}_{0.55}[\text{Ni}_{0.1}\text{Fe}_{0.1}\text{Mn}_{0.8}]\text{O}_2$ exhibited excellent power capability. In particular, even at the extremely high current density of 2400 mA g^{-1} , $\text{P2-Na}_{0.55}[\text{Ni}_{0.1}\text{Fe}_{0.1}\text{Mn}_{0.8}]\text{O}_2$ still delivered

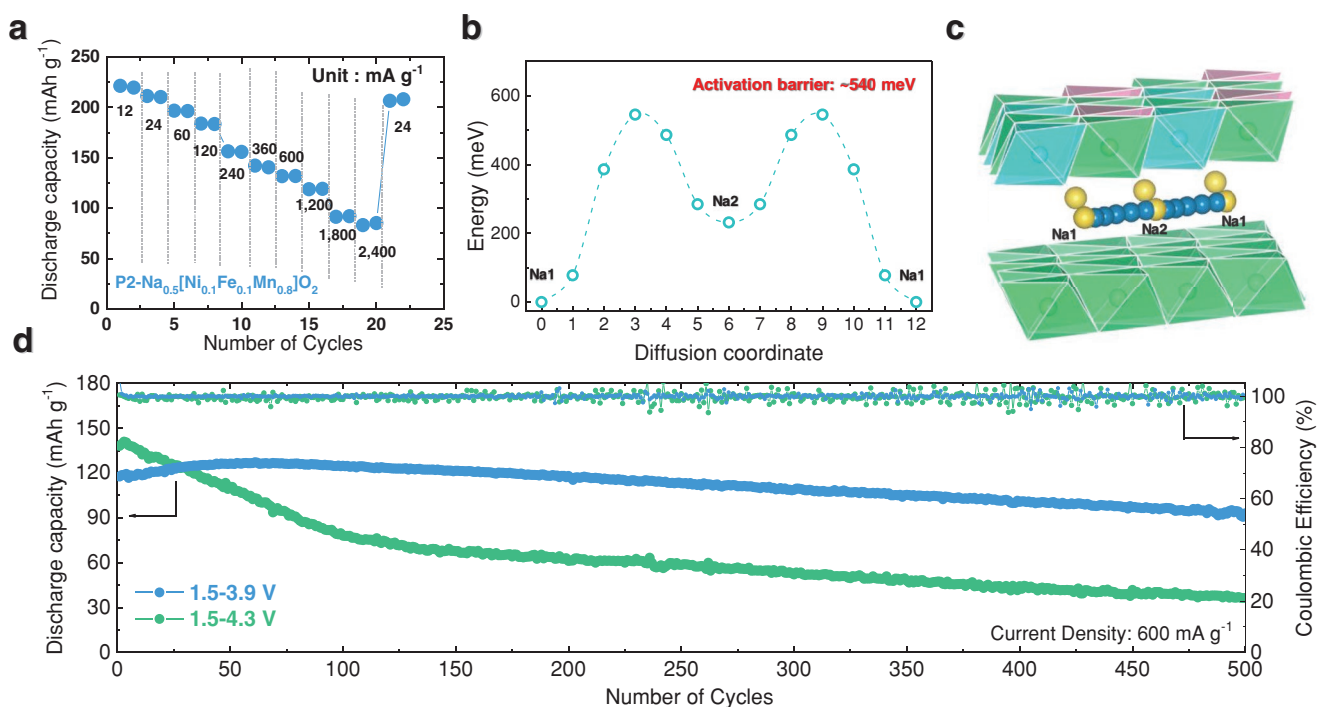


Figure 6. a) Rate capability tests of P2-Na_{0.55}[Ni_{0.1}Fe_{0.1}Mn_{0.8}]O₂ at various current densities from 12 to 2400 mA g⁻¹ in the voltage range of 1.5–4.3 V. b) Na1–Na2–Na1 diffusion pathways in the P2-Na_{0.55}[Ni_{0.1}Fe_{0.1}Mn_{0.8}]O₂ structure. c) NEB calculation of activation barrier energy for Na⁺ diffusion in P2-Na_{0.55}[Ni_{0.1}Fe_{0.1}Mn_{0.8}]O₂. d) Long-term cycling stability tests of P2-Na_{0.55}[Ni_{0.1}Fe_{0.1}Mn_{0.8}]O₂ in 1.5–4.3 and 1.5–3.9 V voltage windows, at a high current density of 600 mA g⁻¹.

a high discharge capacity of 85 mAh g⁻¹; this indicates that P2-Na_{0.55}[Ni_{0.1}Fe_{0.1}Mn_{0.8}]O₂ can sustain adequate power capabilities in SIBs. In general, the power capability of layered oxide cathode materials heavily depends on the mobility of Na⁺ ions in SIBs; in this regard, the reason of the outstanding power capability of P2-Na_{0.55}[Ni_{0.1}Fe_{0.1}Mn_{0.8}]O₂ was investigated through first-principles calculation with the nudged elastic band (NEB) method.^[33] Figure 6c shows that the Na diffusion channels along the Na1–Na2–Na1 path are composed of repeated interconnected units. The calculated activation barrier energy (Figure 6b) for Na⁺ diffusion in the *ab* plane of the P2-Na_{0.55}[Ni_{0.1}Fe_{0.1}Mn_{0.8}]O₂ structure was only ≈540 meV, which enables facile Na diffusion into the structure and proves the high power capability of P2-Na_{0.55}[Ni_{0.1}Fe_{0.1}Mn_{0.8}]O₂. In addition, we compared the activation barrier energy for Na⁺ diffusion between P2-Na_{0.55}[Ni_{0.1}Fe_{0.1}Mn_{0.8}]O₂ and P2-Na_{0.67}MnO₂. Figure S9 in the Supporting Information shows that the predicted activation barrier energy of the P2-Na_{0.67}MnO₂ is ≈582 meV, which is larger than that of the P2-Na_{0.55}[Ni_{0.1}Fe_{0.1}Mn_{0.8}]O₂ (≈540 meV). We suppose that smaller activation barrier energy for Na⁺ ionic diffusion of the P2-Na_{0.55}[Ni_{0.1}Fe_{0.1}Mn_{0.8}]O₂ than that of the P2-Na_{0.67}MnO₂ may result from the existence of Fe and Ni that can suppress the Jahn–Teller distortion of Mn³⁺.

On the other hand, the cycling performance of the P2-type Na_xMeO₂ cathode that underwent P2-OP4 phase transformation during cycling usually showed a marked dependence on the cut-off voltage window. Previous studies showed that although Na⁺ ions can be extracted from the P2-Na_{2/3}MeO₂ structure by increasing the charge potential, multiple phase transformations

usually observed at high charge cut-off potentials resulted in rapid capacity fading and poor rate capability.^[34] Even worse, this phenomenon is more pronounced in long-term cycling tests under high current density conditions. Namely, the P2-OP4 phase transition in the P2-Na_{0.55}[Ni_{0.1}Fe_{0.1}Mn_{0.8}]O₂ structure could not guarantee the use of the material for the high-power application. Therefore, we further optimized the charge cut-off potential to enhance the long-term cycling stability under a high current density. Although charging to 4.3 V enables large capacity and energy density of P2-Na_x[Ni_{0.1}Fe_{0.1}Mn_{0.8}]O₂, it accompanies larger structural change of P2-Na_x[Ni_{0.1}Fe_{0.1}Mn_{0.8}]O₂, such as increase of *c*-lattice parameter and P2-OP4 phase transition. Thus, when P2-Na_x[Ni_{0.1}Fe_{0.1}Mn_{0.8}]O₂ electrode was charged to 3.9 V (without P2-OP4 phase transition), it would experience less structural change compared to P2-Na_x[Ni_{0.1}Fe_{0.1}Mn_{0.8}]O₂ charged to 4.3 V, which enables more outstanding cycle performance of the electrode charged to 3.9 V than that charged to 4.3 V. As shown in Figure 6d, the P2-Na_{0.55}[Ni_{0.1}Fe_{0.1}Mn_{0.8}]O₂ cathode exhibited rapid capacity fading in the expanded voltage window of 1.5–4.3 V because of the repeated P2-OP4 phase transition. In contrast, bypassing the P2-OP4 phase transition, the P2-Na_{0.55}[Ni_{0.1}Fe_{0.1}Mn_{0.8}]O₂ cathode was highly reversible in the voltage range of 1.5–3.9 V, which resulted in an exceptional long-term cycling stability of ≈80% after 500 cycles even at a high current density of 600 mA g⁻¹. Moreover, during repeated charging/discharging, P2-Na_x[Ni_{0.1}Fe_{0.1}Mn_{0.8}]O₂ exhibited the high Coulombic efficiency of more than 99%. Note that the slight increase in capacity during initial 50 cycles during initial 50 cycles may result from the cell stabilization for Na ionic diffusion at high

current density. To obtain a better understanding of the enhanced cycling performance of P2- $\text{Na}_{0.55}[\text{Ni}_{0.1}\text{Fe}_{0.1}\text{Mn}_{0.8}]\text{O}_2$ in a narrow voltage window of 1.5–3.9 V, TEM analyses were further carried out for the cycled P2- $\text{Na}_{0.55}[\text{Ni}_{0.1}\text{Fe}_{0.1}\text{Mn}_{0.8}]\text{O}_2$ cathodes. Figure S10 in the Supporting Information displays bright-field TEM images of cycled P2- $\text{Na}_{0.55}[\text{Ni}_{0.1}\text{Fe}_{0.1}\text{Mn}_{0.8}]\text{O}_2$ with different voltage windows. Surface exfoliation was observed for the cycled electrode in the voltage window of 1.5–4.3 V (Figure S10a, Supporting Information); this possibly involves structural damage and side reactions such as surface oxidation at high voltage.^[35] The corresponding high-resolution TEM image of the damaged surface in Figure S10b in the Supporting Information showed that the layered structure was destroyed and became amorphous at the particle edges.^[36] In contrast, the TEM image of the cycled electrode in the 1.5–3.9 V voltage window shows that pulverization of particles due to prolonged cycling was minimal (Figure S10c–d, Supporting Information). The TEM data of the two postcycling samples (in Figure S10, Supporting Information) suggests that the choice of an optimum operation potential for the P2- $\text{Na}_{0.55}[\text{Ni}_{0.1}\text{Fe}_{0.1}\text{Mn}_{0.8}]\text{O}_2$ cathode can efficiently avoid damage to the crystal structure introduced by repeated P2-OP4 phase transitions and unwanted side reaction during long-term cycling under high-rate conditions. Additionally, we fabricated and performed of P2- $\text{Na}_{0.55}[\text{Ni}_{0.1}\text{Fe}_{0.1}\text{Mn}_{0.8}]\text{O}_2$ full cell using hard-carbon anode at the voltage range between 1.0 and 4.0 V over 100 cycles (Figure S12, Supporting Information), which indicates that P2- $\text{Na}_{0.55}[\text{Ni}_{0.1}\text{Fe}_{0.1}\text{Mn}_{0.8}]\text{O}_2$ exhibited the outstanding electrochemical performances as the promising cathode, under the full-cell system for SIB. Through XPS analysis, we also confirmed that the Mn^{2+} contents at the surface on the hard-carbon anode for the full-cell test was negligible (Figure S11, Supporting Information); this result obviously demonstrated that the P2- $\text{Na}_x[\text{Ni}_{0.1}\text{Fe}_{0.1}\text{Mn}_{0.8}]\text{O}_2$ has a excellent structural stability without Mn dissolution that were usually observed in Mn-based cathode materials in SIBs.

3. Conclusion

In this study, we proposed P2-type $\text{Na}_{0.55}[\text{Ni}_{0.1}\text{Fe}_{0.1}\text{Mn}_{0.8}]\text{O}_2$ as an efficient intercalation host for high energy density SIBs. We optimized the structure of Mn-based P2-type Na_xMeO_2 cathodes through partial substitution of Ni^{2+} and Fe^{3+} into the TM layer. The partial Ni and Fe substitution in Mn sites significantly improved the reversibility of the Na^+ (de)intercalation process with simple electrochemistry. P2- $\text{Na}_{0.55}[\text{Ni}_{0.1}\text{Fe}_{0.1}\text{Mn}_{0.8}]\text{O}_2$ delivered a high discharge capacity of 221.5 mAh g^{-1} with a high average potential of 2.9 V (vs Na/Na^+) and an excellent cycling stability of 75% after 100 cycles. Compared to previously reported layered oxide cathodes, P2- $\text{Na}_{0.55}[\text{Ni}_{0.1}\text{Fe}_{0.1}\text{Mn}_{0.8}]\text{O}_2$ is one of the most attractive cathode material with a high energy density and an average working potential of ≈ 2.9 V (Figure 7). Furthermore, the estimated specific energy density of P2- $\text{Na}_{0.55}[\text{Ni}_{0.1}\text{Fe}_{0.1}\text{Mn}_{0.8}]\text{O}_2$ (based on the weight of positive) reached 350 Wh kg^{-1} ,^[9] which denotes a highly competitive performance compared with those of other layered oxides reported to date. Moreover, the P2- $\text{Na}_{0.55}[\text{Ni}_{0.1}\text{Fe}_{0.1}\text{Mn}_{0.8}]\text{O}_2$ cathode showed excellent power capability; for example, a capacity of 85 mAh g^{-1} was achieved even at a current density of 2400 mA g^{-1} . The overall electrochemical Na

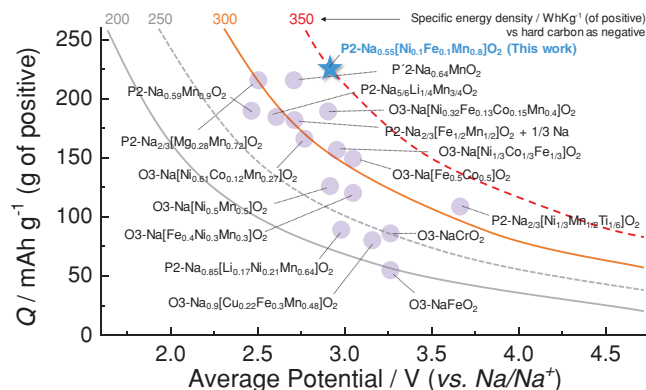


Figure 7. Plots of average voltage versus gravimetric discharge capacity reported for sodium-based layered oxide cathode materials, together with calculated energy density curves. The energy density map of the layered oxide cathode materials, based on the weight of active materials only, was estimated by calculation with the assumption of 350 mAh g^{-1} for hard carbon as a negative electrode material of full cells.

storage mechanism of $\text{Na}_{0.55}[\text{Ni}_{0.1}\text{Fe}_{0.1}\text{Mn}_{0.8}]\text{O}_2$ was investigated using a combination of electrochemical profiles, in operando X-ray diffraction measurements, and first-principles calculation. We believe that the present findings open new avenues in the development of efficient cathode materials in low cost and high energy density sodium-ion batteries.

4. Experimental Section

Synthesis of P2- $\text{Na}_{0.55}[\text{Ni}_{0.1}\text{Fe}_{0.1}\text{Mn}_{0.8}]\text{O}_2$ and P2- $\text{Na}_{0.67}\text{MnO}_2$ Cathode Materials: The P2- $\text{Na}_{0.55}[\text{Na}_{0.1}\text{Fe}_{0.1}\text{Mn}_{0.8}]\text{O}_2$ cathode material was prepared via a typical solid-state method. For the solid-state reaction, stoichiometric amounts of sodium carbonate, nickel (II) acetate tetrahydrate, iron (II) acetate, and manganese (II) acetate tetrahydrate were mixed according to the desired Na:Ni:Fe:Mn ratios. The mixed powders were calcined at 950°C for 12 h in O_2 atmosphere and then quenched in Ar atmosphere. For comparison, P2- $\text{Na}_{0.67}\text{MnO}_2$ was synthesized via same synthesis process. In details, stoichiometric amounts of sodium carbonate and manganese (II) acetate tetrahydrate were mixed according to the desired Na:Mn ratios and the mixed powders were calcined at 1000°C for 12 h in O_2 atmosphere and then quenched in Ar atmosphere.

Analytical Techniques: The crystalline phases of the synthesized materials were characterized by powder XRD (Rint-2000, Rigaku, Japan) using $\text{Cu K}\alpha$ radiation. The FullProf Rietveld program was used to analyze the powder diffraction patterns. The in operando synchrotron XRD experiments were performed at the 6D beamline of the Pohang Accelerator Laboratory (PAL) in Pohang, Korea. The wavelength ($\lambda = 0.65303 \text{ \AA}$) of the incident beam and the sample-detector distance were calibrated using a LaB_6 standard. A modified 2032 coin-type half-cell with a 3 mm diameter hole at its center containing a Kapton window served as the X-ray beam path. While the cell was being charged by applying a constant current of 12 mA g^{-1} , the XRD patterns were continuously recorded with a 2D charge-coupled device detector (MX225-HS, Rayonix) in transmission mode. The 2θ angles of all XRD patterns were converted to those of a conventional X-ray tube with $\lambda = 1.5406 \text{ \AA}$ ($\text{Cu K}\alpha$ radiation) for easy comparison. The particle morphology and composition were investigated using TEM (JEM2010, JEOL) and EDX (JEM 2100F, JEOL) measurements. The atomic ratios of the elements were determined using ICP (Polyscan 60E, Thermo Jarrell Ash, Franklin, MA, USA). XPS (PHI5600, Perkin-Elmer, USA) measurements in macro

mode (3 mm × 3 mm) were performed to determine the oxidation state of the transition metal ions. During the XPS measurements, the samples were first placed into a hermetically sealed transfer chamber in a glovebox and then transferred into the vacuum chamber of the XPS instrument, preventing exposure to air or water.

Electrochemical Tests: The cathodes were fabricated by blending the active materials (85 wt%), Super P carbon black (10 wt%), and polyvinylidene fluoride (5 wt%). The resulting slurry was applied onto aluminum foil and dried at 110 °C for 12 h in a vacuum oven. Then, disks were punched out of the foil (electrode size: 14 φ, average loading amount of active materials: 3.0 mg cm⁻²). Electrochemical tests were conducted using a 2032 coin-type cell; all cells were prepared in an Ar-filled dry box. Na metal was used as anode, whereas the electrolyte solution consisted of 0.5 M NaPF₆ in propylene carbonate (PC) and fluoroethylene carbonate (FEC) (98:2 by volume). The cells were typically tested in constant current mode, within a voltage range of 1.5–4.3 V versus Na/Na⁺.

Computational Details: DFT calculations were performed using the Vienna ab initio simulation package (VASP).^[37] Projector-augmented wave (PAW) pseudopotentials^[38] were used with a plane-wave basis set, as implemented in VASP. The Perdew–Burke–Ernzerhof (PBE) parametrization of the generalized gradient approximation (GGA) was used for the exchange–correlation function.^[39] The GGA+U method^[40] was adopted to address the localization of d-orbitals in Mn, Fe, and Ni ions, with U values of 3.9, 4.0, and 6.0 eV, respectively, as determined in previous reports.^[41] All calculations were performed with an energy cutoff of 500 eV until the residual forces in the system converged to less than 0.05 eV Å⁻¹ per unit cell. The phase stability of the P2- and OP4-Na_x[Na_{0.1}Fe_{0.1}Mn_{0.8}]O₂ compounds was investigated by generating all Na configurations corresponding to specific Na contents and calculating the formation energies. The cluster-assisted statistical mechanics (CASM) software was used for the generation of all Na/vacancy configurations for each composition; this was followed by full DFT calculations on a maximum of 30 configurations with the lowest electrostatic energy for each composition, to obtain a convex hull plot for P2- and OP4-Na_x[Na_{0.1}Fe_{0.1}Mn_{0.8}]O₂.^[42] NEB calculations^[33] were performed to determine the activation barrier for Na⁺ diffusion in the Na_x[Na_{0.1}Fe_{0.1}Mn_{0.8}]O₂ structure. A unit cell created by five formula units of P2-Na_x[Na_{0.1}Fe_{0.1}Mn_{0.8}]O₂ with one generated vacancy was used to model the Na⁺ diffusion. Five intermediate states were considered between the first and final images of a single Na⁺ diffusion event. During the NEB calculation, all structures were allowed to relax with fixed lattice parameters.

Supporting Information

Supporting Information is available from the Wiley Online Library or from the author.

Acknowledgements

J.-Y.H. and J.K. contributed equally to this work. This work was supported by the Global Frontier R&D Program (No. 2013M3A6B1078875) of the Center for Hybrid Interface Materials (HIM), funded by the Ministry of Science, ICT, and Future Planning; further support was provided by the Human Resources Development program (No. 20184010201720) of the Korea Institute of Energy Technology Evaluation and Planning (KETEP), funded by the Ministry of Trade, Industry, and Energy of the Korean government.

Conflict of Interest

The authors declare no conflict of interest.

Keywords

high-capacity, high energy density, high-rate, P2-type cathodes, sodium-ion batteries

Received: October 30, 2018

Revised: January 19, 2019

Published online: February 25, 2019

- [1] B. Scrosati, J. Hassoun, Y.-K. Sun, *Energy Environ. Sci.* **2011**, 4, 3287.
- [2] K. Turcheniuk, D. Bondarev, V. Singhal, G. Yushin, *Nature* **2018**, 559, 467.
- [3] J.-Y. Hwang, S.-T. Myung, Y.-K. Sun, *Chem. Soc. Rev.* **2017**, 46, 3529.
- [4] P.-F. Wang, H.-R. Yao, X.-Y. Liu, Y.-X. Yin, J.-N. Zhang, Y. Wen, X. Yu, L. Gu, Y.-G. Guo, *Sci. Adv.* **2018**, 4, eaar6018.
- [5] Y. Xiao, P.-F. Wang, Y.-X. Yin, Y.-F. Zhu, X. Yang, X.-D. Zhang, Y. Wang, X.-D. Guo, B.-H. Zhong, Y.-G. Guo, *Adv. Energy Mater.* **2018**, 8, 1800492.
- [6] C. Delmas, *Adv. Energy Mater.* **2018**, 8, 1703137.
- [7] X. Rong, E. Hu, Y. Lu, F. Meng, C. Zhao, X. Wang, Q. Zhang, X. Yu, L. Gu, Y.-S. Hu, H. Li, X. Huang, X.-Q. Yang, C. Delmas, L. Chen, *Joule*, **2019**, 3, 1.
- [8] R. J. Clément, P. G. Bruce, C. P. Grey, *J. Electrochem. Soc.* **2015**, 162, A2589.
- [9] S. Kumakura, Y. Tahara, K. Kubota, K. Chihra, S. Komaba, *Angew. Chem., Int. Ed.* **2016**, 55, 12760.
- [10] J. Billaud, G. Singh, A. R. Armstrong, E. Gonzalo, V. Roddatis, M. Armand, T. Rojo, P. G. Bruce, *Energy Environ. Sci.* **2014**, 7, 1387.
- [11] J. M. Paulsen, J. R. Dahn, *Solid State Ionics* **1999**, 126, 3.
- [12] R. Stoyanova, D. Carlier, M. Sendova-Vassileva, M. Yoncheva, E. Zhecheva, D. Nihtianova, C. Delmas, *J. Solid State Chem.* **2010**, 183, 1372.
- [13] N. Yabuuchi, R. Hara, M. Kajiyama, K. Kubota, T. Ishigaki, A. Hoshikawa, S. Komaba, *Adv. Energy Mater.* **2014**, 4, 1301453.
- [14] Z. Lu, J. Dahn, *J. Electrochem. Soc.* **2001**, 148, A1225.
- [15] A. Konarov, J. Y. Choi, Z. Bakenov, S.-T. Myung, *J. Mater. Chem. A* **2018**, 6, 8558.
- [16] N. Yabuuchi, M. Kajiyama, J. Iwatate, H. Nishikawa, S. Hitomi, R. Okuyama, R. Usui, Y. Yamada, S. Komaba, *Nat. Mater.* **2012**, 11, 512.
- [17] R. J. Clément, J. Billaud, A. R. Armstrong, G. Singh, T. Rojo, P. G. Bruce, C. P. Grey, *Energy Environ. Sci.* **2016**, 9, 3240.
- [18] T. Roisnel, J. Rodriguez-Carvajal, *FullProf Manual*, Institute Laue-Langevin, Grenoble, France **2002**.
- [19] C. Delmas, J.-J. Braconnier, C. Fouassier, P. Hagenmuller, *Solid State Ionics* **1981**, 3–4, 165.
- [20] A. Davidson, J. F. Tempere, M. Che, *J. Phys. Chem.* **1996**, 100, 4919.
- [21] F. Wu, J. Tian, Y. Su, J. Wang, C. Zhang, L. Bao, T. He, J. Li, S. Chen, *ACS Appl. Mater. Interfaces* **2015**, 7, 7702.
- [22] J. Guo, X. Zhang, X. Du, F. Zhang, *J. Mater. Chem. A* **2017**, 5, 6447.
- [23] C. V. Ramana, M. Massot, C. M. Julien, *Surf. Interface Anal.* **2005**, 37, 412.
- [24] T. Yamashita, P. Hayes, *Appl. Surf. Sci.* **2008**, 254, 2441.
- [25] R. Rajagopalan, B. Chen, Z. Zhang, X.-L. Wu, Y. Du, Y. Huang, B. Li, Y. Zong, J. Wang, G.-H. Nam, M. Sindoro, S. X. Dou, H. K. Liu, H. Zhang, *Adv. Mater.* **2017**, 29, 1605694.
- [26] G. Singh, J. M. L. Amo, M. Galceran, S. Pérez-Villar, T. Rojo, *J. Mater. Chem. A* **2015**, 3, 6954.
- [27] D. Yuan, X. Hu, J. Qian, F. Pei, F. Wu, R. Mao, X. Ai, H. Yang, Y. Cao, *Electrochim. Acta* **2014**, 116, 300.

- [28] G. Singh, N. Tapia-Ruiz, J. M. L. D. Amo, U. Maitra, J. W. Somerville, A. R. Armstrong, J. M. Ilarduya, T. Rojo, P. G. Bruce, *Chem. Mater.* **2016**, *28*, 5087.
- [29] G. G. Amatucci, J. M. Tarascon, C. Kleinb, *J. Electrochem. Soc.* **1996**, *143*, 1114.
- [30] A. Van der Ven, M. K. Aydinol, G. Ceder, *J. Electrochem. Soc.* **1998**, *145*, 2149.
- [31] S. Komaba, N. Yabuuchi, T. Nakayama, A. Ogata, T. Ishikawa, I. Nakai, *Inorg. Chem.* **2012**, *51*, 6211.
- [32] R. Berthelot, M. Pollet, D. Carlier, C. Delmas, *Inorg. Chem.* **2011**, *50*, 2420.
- [33] G. Henkelman, *J. Chem. Phys.* **2000**, *113*, 9901.
- [34] J. S. Thorne, R. A. Dunlap, M. N. Obrovac, *J. Electrochem. Soc.* **2014**, *161*, A2232.
- [35] Y. Liu, X. Fang, A. Zhang, C. Shen, Q. Liu, H. Enaya, C. Zhou, *Nano Energy* **2016**, *27*, 27.
- [36] J.-Y. Hwang, S.-T. Myung, C. S. Yoon, S.-S. Kim, D. Aurbach, Y.-K. Sun, *Adv. Funct. Mater.* **2016**, *26*, 8083.
- [37] G. Kresse, J. Furthmüller, *Comput. Mater. Sci.* **1996**, *6*, 15.
- [38] P. E. Blöchl, *Phys. Rev. B* **1994**, *50*, 17953.
- [39] J. P. Perdew, K. Burke, M. Ernzerhof, *Phys. Rev. Lett.* **1996**, *77*, 3865.
- [40] V. I. Anisimov, F. Aryasetiawan, A. I. Lichtenstein, *J. Phys.: Condens. Matter* **1997**, *9*, 767.
- [41] A. Jain, G. Hautier, S. P. Ong, C. J. Moore, C. C. Fischer, K. A. Persson, G. Ceder, *Phys. Rev. B* **2011**, *84*, 045115.
- [42] A. Van der Ven, J. C. Thomas, Q. Xu, J. Bhattacharya, *Math. Comput. Simul.* **2010**, *80*, 1393.